Materials Science and Engineering B 320 (2025) 118425

Contents lists available at ScienceDirect

Materials Science & Engineering B

journal homepage: www.elsevier.com/locate/mseb

Assessing pseudocapacitive and OER-HER electrocatalytic potential of bimetallic Copper-Nickel/Graphene oxide nanocomposite

Kedar Sahoo [a,*], Deepak Kumar [b], Vishal K. Kushwaha [b], Ajinkya Kotkar [a], Arindam Indra [b], Shirish H. Sonawane [c], Suddhasatwa Basu [a,*]

[a] Chemical Engineering Department, IIT Delhi, New Delhi, India
[b] Department of Chemistry, IIT (BHU), Varanasi, U.P., India
[c] Chemical Engineering Department, NITW Telangana, India

ARTICLE INFO

Keywords:
Multimetallic oxide
Nanocomposite
Supercapacitor
OER
HER

ABSTRACT

Copper-nickel oxide/GO (CNO/GO) nanocomposite was synthesized via a low-temperature thermal reduction technique with crystallographic phase matching with an off-stoichiometric type $Cu_{0.05}Ni_{0.95}O$/GO structure. Three-electrode-based electrochemical experiments suggest that the prepared CNO/GO nanocomposite can store energy via the pseudocapacitive mechanism. The charge storage efficacy is also reflected in the high-power density value (~267 W/kg) achieved at a current density of 1 A/g compared to earlier reported nickel oxide-based composites. The practical performance of the CNO/GO nanocomposite can be corroborated by the fact that in a symmetric coin cell device, it results in a specific capacity of ~37F/g @ 1A/g and retains its ~84 % specific capacity after 8000 cycles. The flexibility of using CNO/GO nanocomposite as an exceptional electrocatalytic material can be recognized from the smaller overpotential (η) values, e.g., 340 mV and 359 mV for OER and HER, respectively, in conjunction with chronoamperometric stability retained over 24 h. All these multiple electrochemical attributes establish the potential of using CNO/GO nanocomposite in energy storage and conversion.

1. Introduction

Under the guise of diverting focus upon a larger dependency on fossil-derived fuels of growing stress on the environment and economy, there has been a paradigm shift toward renewable energy generation and storage [1,2]. The storage of renewable energy can be accomplished via electrochemical devices (battery, supercapacitor, etc.), and can be generated via electrochemical water splitting [3,4]. From the energy storage perspective, supercapacitors are better compared to batteries in terms of their power density, charge storage rate, and cyclability [5]. Similarly, electrochemical water splitting remains advantageous from the perspective of producing a cleaner and greener form of energy, "hydrogen (H_2)" [6].

In supercapacitors as well as electrochemical water splitting, the selection of a suitable electrode/electrocatalyst material is crucial, since they actively participate in electrochemical conversion [7].

Generally, carbonaceous materials, e.g., activated carbon, carbon nanotubes, graphene, etc., are the popular electrode materials in supercapacitors where the electrochemical charge storage proceeds via physical adsorption-desorption of ions (EDLC mechanism) [8]. Graphene oxide (GO), by its good specific surface area (>2500 m^2/g), oxygen functionalities, electron mobility, and thermo-mechanical properties, is superior among the studied carbonaceous electrode materials for application in supercapacitors [9–12]. However, their applicability is limited due to a lack of specific capacity delivery. Contrary to graphene oxide, transition metal oxides, via their redox transitions when used as electrode material in supercapacitors, deliver high specific capacity, good energy density, and excellent rate capability. Based on this, many studies have adopted transition metal oxides as a supercapacitive material for electrochemical charge storage [13]. Presently, there is a trend of utilizing bimetallic transition metal oxide structures as electrode material in high-performance supercapacitors [14,15]. The co-existence of multiple metal cations in the composition fetches more electrons during the redox transitions in charge storage. As a result, there is an increase in the electrical conductivity, a reduction in the charge transfer impedance, and an overall improvement in the

* Corresponding authors.
E-mail addresses: kedarsahoo007@gmail.com (K. Sahoo), sbasu@chemical.iitd.ac.in (S. Basu).

https://doi.org/10.1016/j.mseb.2025.118425
Received 6 October 2024; Received in revised form 22 April 2025; Accepted 11 May 2025
Available online 15 May 2025

supercapacitive performance [14,16]. Furthermore, properties like reduction in the overall density of the material, high electrolyte exposure, and large ion diffusion pathways are some associated advantages during the use of bi-metallic oxides during electrochemical reactions [17–19].

Similar to electrochemical charge storage, the utilization of bi-metallic oxides could be effective in catalyzing electrochemical oxidation-reduction reactions for the water-splitting process [20]. Bi-metallic oxides have multiple valence states at the cation occupancy level in octahedral or tetrahedral positions [21]. Variation in the valence state of cations leads to the formation of donor-acceptor sites for the adsorption of oxygen ions, and the thermodynamically difficult oxygen-evolution reaction involved in the water electrolysis could be easily accomplished [22]. Additionally, bi-metallic oxides could also lower the activation energy involved in the electrolysis process via the electron hopping mechanism [23,24]. Further, multiple transition metals involved in the bi-metallic oxides are promising for providing good electrochemical activity, stability, and overpotential value compared to their monometallic counterparts [25].

A bi-metallic oxide structure made out of the combination of transition metal oxides of nickel and copper could be a viable option for showcasing simultaneous electrochemical activity based on properties like easy availability, low cost, non-toxicity, prominence in electroactive site dominance, and good theoretical capacitance [26–28]. In fact, in the popularly adopted alkaline electrolytic mediums, bi-metallic oxide structures made out of nickel and copper are superior to platinum, iridium, and ruthenium-based electrocatalysts from cost, safety, stability, purity, corrosion inhibition prospects [29,30].

However, the bimetallic oxide structures have some limitations in terms of high specific area, thermo-mechanical stability, and porosity [3,31]. By synergistically combining GO and copper-nickel bi-metallic oxide, there could be complementation of each other's drawbacks. The transition metals break the electro-neutrality within graphene, and reversibly, GO provides requisite surface area, conductivity, and stability [25].

There are previous reports on several bimetallic oxides-GO nanocomposites in electrochemical energy storage as well as in electrocatalysis, such as Co_3O_4@RuO_2/Graphene [32], CuO/NiO/N-rGO [33], Graphene@MoS_2@TiO_2 [34], Co–Mn oxide/graphene [35], GO-MnNi [36], Bimetallic MOF@GO [37], GO/$La_2Ti_2O_7$ [38], $NiCo_2O_4$ & $CuCo_2O_4$/rGO [39], $Ni_{1-x}Cu_xFe_2O_4$@rGO [40], $NiMn_2O_4$/rGO [41], Cu-doped $NiCo_2O_4$ [42], $Cu_xCo_{3-x}O_4$/N-rGO [43], etc. However, the studies on the nanocomposites of copper-nickel oxide with graphene are the least reported, especially in the areas of energy storage and electrocatalysis. Balamurgan et al. [44] demonstrated the solvothermal synthesis of Cu-Ni oxide, forming a composite with N-doped graphene for supercapacitive energy storage under 6 M KOH electrolytic conditions. In another work by Mohana et al. [45] reports the electrocatalytic performance of CuO/NiO/rGO nanocomposite synthesized via the co-precipitation method. Nguyen et al. [46] electrochemically synthesized a composite of graphene sheets decorated with nickel/copper oxides anchored on polyaniline for electrochemical sensing of methanol. In another study, Liu et al. [47] fabricated a CuO-Nio/Graphene composite for the electrochemical detection of dopamine, acetaminophen, and tryptophan. All such reports highlight the synergistic role of formed composites in augmenting the electrochemical activities. Still, the amount of reported works in this area is limited.

Ramesh et al. [9] in their recently published article highlight the active use of Cu/Ni-oxide & N-doped GO for electrochemical energy in a symmetric cell configuration. Inspired by their work, the current study has been designed and performed to extract diverse electrochemical functionalities out of the synthesized nanocomposite of Cu/Ni-oxide and GO. This study has its novelty in terms of its modified synthesis method and exhibition of diverse functionalities of Cu-Ni Oxide/GO nanocomposite in electrochemical energy storage as well as in OER-HER electrocatalysis, which is hardly reported anywhere.

2. Experimental:

Modified Hummer's method was adopted for the synthesis of Graphene oxide (GO). A detailed GO synthesis process is provided in the electronic supplementary information (Section S1, ESI). Briefly describing 0.8 g of GO powder was homogenized in 250 mL of DI water via the application probe sonication method (Helix Biosciences, HBSNII92, 1h, 0.5 Hz frequency). Two aqueous phase solutions (each 0.1 M concentration) were prepared by dissolving salts of copper nitrate ($Cu(NO_3)_2.5H_2O$) and nickel chloride ($NiCl_2.6H_2O$) purchased from SDFCL, India, in 250 mL of DI water. Both solutions are mixed by the action of magnetic stirring and subjected to reaction at a temperature of 90 ^oC. Since this work is influenced by and modifications of earlier research reported by Ramesh et al. [9] on the development of bimetallic oxide-GO composite for energy storage applications, no additional efforts were made to vary the molar ratio of precursor salts. All the concentrations taken over here are in optimal amounts as per the adaptation. Additionally, to the reacting solution mixture, 1 g of polyvinylpyrrolidone (Himedia, K-40, India) and 40 mL of ammonia solution (25 % assay, Himedia, India) were added. Finally, overall reaction proceeded over a 12h period, and the resulting nanocomposite was collected via repeated washing under centrifugation and sonication. The purified nanocomposite was calcined overnight at 450 ^oC and stored. The schematic synthesis procedure of the multimetallic/GO nanocomposite is demonstrated in Fig. 1.

The X-ray crystallographic analysis of the prepared nanocomposite was carried out in a Rigaku Smart Lab diffractometer (CuKα radiation source). The optical property was measured in a Raman spectrometer (STR-300, 633 nm laser excitation). Detailed morphology and electronic diffraction patterns were ascertained by a high-resolution scanning electron microscope (FEI NOVA NANOSEM 450, USA) and a high-resolution transmission electron microscope (FEI TECNAI G^2 20 TWIN), respectively. The oxidation states of constituent elements of the prepared composite were examined via X-ray photoelectron spectroscopy (AMICUS, Kratos Analytical). The detailed chemical composition was examined by FTIR spectroscopy (Thermo Electron Corporation, USA). The concentration of metallic species involved in the synthesized composite was further investigated via the atomic absorption spectroscopy (AAS) technique (ZEEnit700p, analytikjena, Germany).

The electrochemical characteristics of the prepared nanocomposite were examined in a three-electrode probe electrochemical workstation (Metrohm Autolab M204). The electrode system comprised Ag/AgCl as a reference electrode with prepared composite and platinum (Pt) acting as working and counter electrodes, respectively. The synthesized nanocomposite (~1 mg) was dispersed in a 500 μL volume, where 20 μL of Nafion additive acted as a binder. The prepared suspension was carefully drop-cast on a Ni foam (1×1 cm^2) and oven-dried to act as the working electrode. The electrochemical experiments were carried out in a 1M KOH alkali electrolyte. The electrochemical impedance characteristic was studied under 500 mV AC applied voltage over a 100 kHz to 0.01 Hz frequency range. The electrochemical active surface area (ECA) was

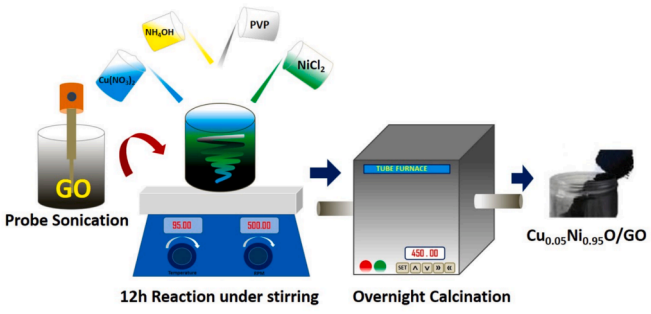

Fig. 1. Schematic synthesis of Copper-Nickel oxide composite with GO.

determined from electrical double-layer capacitance (C_{dl}) measured in the non-faradic region. The galvanostatic charge-discharge (GCD) experiment was performed in a varied current density range of 1-10 A/g.

Further performance benchmarking was done in a two-electrode symmetric cell via the fabrication of a coin cell device and subsequent electrochemical characterizations. A suspension of nanocomposite, carbon black (99.9 %, Alfa Aesar, U.S.), and Polyvinylidene fluoride (Alfa Aesar, U.S.) in an 8:1:1 mass ratio by using N-methyl-2-pyrrolidone (99 %, Alfa Aesar, U.S.) solvent. The painted suspension on a carbon paper substrate was arranged symmetrically to fabricate a CR2032 coin cell. In this coin cell, 1 M KOH and glass fiber acted as electrolyte and separator material, respectively.

3. Results & Discussion

3.1. Physicochemical characteristics of the nanocomposite:

The high-resolution X-ray diffraction analysis (Fig. 2a) shows the crystalline nature of the prepared nanocomposite with highly intense peaks (2θ: 37.21°, 43.23°, 51.72°, 62.94°, 75.40°, 79.38°) that exactly match the standard JCPDS card no. 01-078-0644. According to JCPDS, information synthesized composite can be identified as nickel-copper oxide ($Cu_{0.05}Ni_{0.95}O$), forming a composite with GO. Together, the prepared nanocomposite can henceforth be coined as CNO/GO. The calculated lattice parameter is evaluated to be 4.176 Å, which exactly matches the standard value mentioned in the JCPDS file corresponding to a cubic phase symmetry. The identified major peaks match with the NiO standard pattern (JCPDS card no. 47-1049) while smaller identified peaks match with the monoclinic CuO phase (JCPDS card no. 01-080-0076). This could be the reason for an off-stoichiometric type composition [48]. The very minute variation in the lattice parameter (if any) could be due to the successful formation of a bimetallic composite structure, where simultaneously grown CuO substitutes interstitial sites of NiO [49,50]. However, the absence of characteristic peaks corresponding to prepared graphene oxide (12.4°, 23.29°, 42.59°), in the composite structure, could have been due to the prevention of restacking of the carbon basal plane by probe sonication during the synthesis process [51].

The average crystallite size of the synthesized $Cu_{0.05}Ni_{0.95}O$ nanocomposite is evaluated in terms of the Scherrer equation (Eq. (1) [52].

$$D = \frac{k \times \lambda}{\beta \times \cos\theta} \quad (1)$$

where D = Crystallite size (nm), k = 0.9 (constant adopted for shape

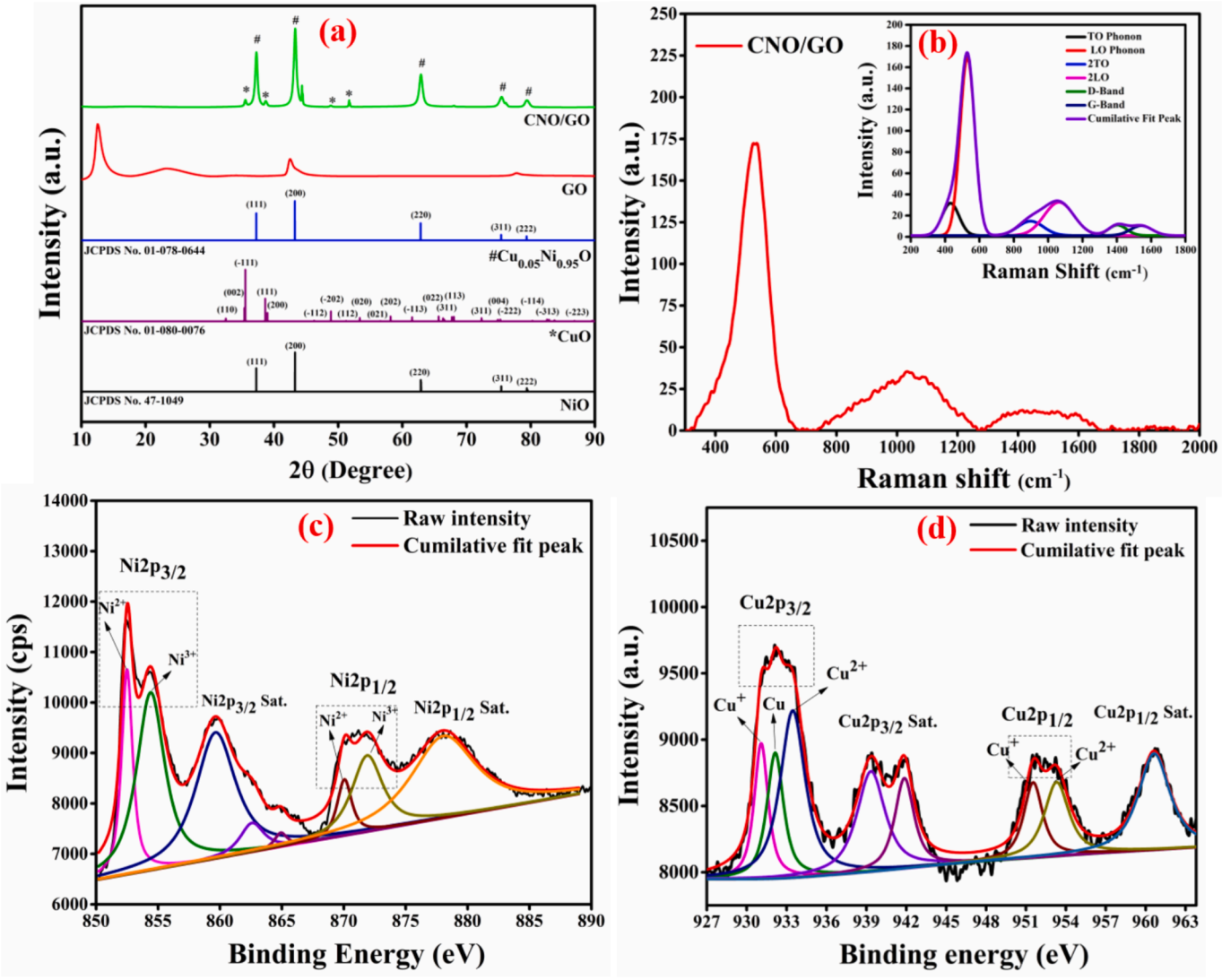

Fig. 2. Crystallographic & spectroscopic analysis of synthesized nanocomposite (a) X-Ray diffraction analysis, (b) Raman spectroscopy, (c) Ni 2p XPS spectra, (d) Cu 2p XPS spectra.

factor), λ = 0.15406 (CuKα wavelength radiation), β = FWHM (radian unit), θ = Bragg angle (radian). Accordingly, the average crystallite size of the prepared $Cu_{0.05}Ni_{0.95}O$ composite is evaluated to be ~15.5 nm.

The Raman spectra of CNO/GO nanocomposite shown in Fig. 2b, indicate the presence of multiple peaks in between 200-1800 cm^{-1} range. The two Raman peaks situated at ~432 and 533 cm^{-1} correspond to transverse optical (TO) and longitudinal optical (LO) first-order phonon vibrations of NiO [53]. Another two peaks located at ~894 and ~1065 cm^{-1} indicate second-order phonon scattering 2TO and 2LO, respectively, corresponding to the same NiO. Since the peaks have been shifted to a higher wavenumber, it indicates the formation of a nanocomposite structure with CuO ($Cu_{0.05}Ni_{0.95}O$). The inelastic scattering of GO content in the nanocomposite under laser irradiation resulted in vibrational peaks at a higher wavenumber range (1100-1800 cm^{-1}). D band is the characteristic of breathing of the j-point phonons of A_{1g} symmetry that is observed ~1400 cm^{-1} [54]. Whereas, the G vibration band associated with first-order scattering of E_{2g} phonons of sp^2 carbon (C-C bond stretching) of graphene is observed at ~1547 cm^{-1}. The incorporation of oxygen functional groups in the carbon basal plane also leads to the observation of the G-band [9]. The integrated intensity ratio ($R=I_D/I_G$) of the D-band and G-band in the prepared graphene oxide material is evaluated to be 0.91. This closely resembles the value suggested by Hidayah et al. [54] for graphene oxide. In the case of raw graphite, this value is reported to be 0.54. [55]. This clearly shows adopted Hummer's method in this present research is successful in the graphitization process.

The valence state, as well as the composition of elements constituting the CNO/GO composite, was examined via the X-ray Photoelectron spectroscopy (XPS) method. This analysis shows that within the surveyed binding energy range, all the respective peaks assigned to the existence of Cu, Ni, C, and O atoms have % compositions of 3.8, 24.1, 31.2, and 40.9, respectively (Fig. S1a). The relative wt.% of each element in the composite was ascertained via a technique suggested by Modafferi et al. [56] utilizing the atomic% data given in the survey spectra. Accordingly, the relative wt.% of Cu and Ni metal in the bimetallic oxide is found to be 5.2 % and 30.1 %, respectively. This indicates the formation of an off-stoichiometric kind of structure of the composition, as suggested by XRD.

The same can also be supported from the AAS data, revealing the concentration (wt.%) of individual metals, i.e., Cu and Ni of 7.7 and 31.6 %, respectively.

The observed core-XPS spectra in the 2p (Ni & Cu) and 1s (C & O) regions are Gaussian fitted. The fitting of the C1s spectra (Fig. S1b) resulted in 3 major peaks, situated at binding energies of 283.65, 285.08, and 287.24 eV, corresponding to C-C, C-O, and C=O bonds, respectively [57,58]. The skeletal structure of oxygen functional groups associated with carbon spectra indicates the successful incorporation of GO into a synthesized composite. The core XPS spectra of Ni 2p upon fitting (Fig. 2c) show two major multiple splits, namely $Ni2p_{3/2}$ and $Ni2p_{1/2}$, situated at binding energy regions of 850.68-856.65 eV and 868.68-873.85 eV, respectively. The multiple split peaks are the reason for the unfilled d-orbital of nickel [48]. The corresponding shakeup satellite peaks of $Ni2p_{3/2}$ and $Ni2p_{1/2}$ are located at binding energies of ~860 eV and ~878 eV, respectively [59]. The presence of both major & satellite peaks is characteristic of Ni^{2+} & Ni^{3+} oxidation states of spin-orbit levels of NiO [60]. Similarly, high-resolution XPS of Cu2p (Fig. 2d) indicates two spin-orbital doublets of the copper element present in the nanocomposite. There are two major peaks present at binding energy values of 932.19 and 952.38 eV (approximately 20 eV apart), corresponding to $Cu2p_{3/2}$ and $Cu2p_{1/2}$ spin orbitals, respectively [5,61]. Highly resolved spin orbitals Cu $2p_{3/2}$ and Cu $2p_{1/2}$ could be assigned both for CuO and/or Cu_2O phases. But the existence of shake-up satellite peaks at ~939.35, ~941.85 eV for $Cu2p_{3/2}$, and at ~960.69 eV for $Cu2p_{1/2}$ orbitals is an indication of divalent state (Cu^{2+}) in the prepared nanocomposite. The satellite peaks are associated with the ground state $3d^9$ configuration of the Cu^{2+} oxidation state of CuO [62]. In the case of Cu_2O and Cu metal, the satellite peak intensities are very minimal due to the filled d-shell [63]. Thus, the synthesized nanocomposite has a majority of CuO phase. Further, due to the absence of LMM-2 auger transitions near 570 eV binding energy in the survey spectra, the slight occurrence of Cu_2O/Cu metal cannot be ruled out under X-ray-induced reduction [48]. The intermingling chemical states of two oxide phases (NiO and CuO) during growth might have some effect on the resulting multiple oxidation states.

High-resolution oxygen 1s spectra (O1s) are identified to consist of two major peaks positioned at ~528.06 and a small peak at ~530.30 eV binding energies (Fig. S1c). The peak corresponding to 528.06 eV is reflected because of lattice oxygen (O^{2-} anion) associated with the M-O-M linkage. The second peak, corresponding to 530.30 eV, accounts for oxygen defects (O^{2-}/O^{-}) present in the nanocomposite. Hence, the observance of multiple oxidation states of Ni and Cu elements in the nanocomposite is well predicted.

Overall, XPS analysis suggested the concurrently grown NiO and CuO phases in the GO matrix during synthesis, ultimately resulting in $Cu_{0.05}Ni_{0.95}O$/GO nanocomposite.

The organic functionality determination of CNO/GO via FTIR analysis is an essential characterization tool for the compositional characteristics. The identified result of FTIR spectroscopy is represented in Fig. S2. The transmittance bands in the fingerprint region: 1000-1130 cm^{-1}, ~1381 cm^{-1}, and ~1629 cm^{-1}, correspond to oxygen-containing functional groups of nanocomposites, e.g., C-O stretching, C-OH deformation, and C=O stretching, respectively. These are indications of graphene in an oxidized form in the prepared nanocomposite [10]. The CH stretching of sp^3 hybridized carbon is represented by weak % transmittance peaks in the region between 2800-3000 cm^{-1} [10]. The broad and intense transmittance peaks observed between 3100-3800 cm^{-1} correspond to OH stretching vibrations that are associated with absorbed water molecules in GO [64]. This can also be interlinked with the COOH oxygen-containing functional group in the fingerprint region (~1629 cm^{-1}) [65]. The additional transmittance peak ~2321 cm^{-1} is the consequence of bonding between GO and CO_2 during synthesis [66]. The sharp transmittance peak reflected below wavenumber 1000 cm^{-1} is an indication of the formation of metal-oxygen-metal bonding during composite growth [5]. All these functional groups support the ascertained compositional structure of $Cu_{0.05}Ni_{0.95}O$/GO nanocomposite.

The morphology of the synthesized CNO/GO nanocomposite was preliminarily ascertained via a field-emission scanning electron microscope (FE-SEM). The microscopic image (Fig. 3a) shows that there is a formation of clusters of asymmetric nanoparticles, with each subunit sized ~18 nm. Scanning electron microscopic images acquired at different magnifications are shown in Fig. S3 in support of this type of observation. Further, the heavily grown agglomerated structures overshadow the simultaneously grown graphene oxide sheets underneath them (Fig. S3). The clustering could have been due to the small size of nanoparticles with high surface energy [5]. Herein, they can be described as agglomerated nanospheres of CNO/GO composite. Further, the TEM magnified image in Fig. 3b confirms the formation of an agglomerated structure. Further, the EDX mapping image shown in Fig. 4 indicates the existence of associated elements (e.g. Cu, Ni, O, C) of the CNO/GO composite without any impurity.

The selected area diffraction pattern (SAED) shows the polycrystallinity involved in the agglomerated nanospheres composite (Fig. 3c). The diffraction pattern closely matches the crystallinity data of CNO/GO. Similarly, from the HR-TEM image shown in Fig. 3d, it can be observed that the width of lattice fringes matches the (111) crystal plane geometry associated with $Cu_{0.05}Ni_{0.95}O$.

3.2. *Electrochemical study using 3-electrode assembly:*

To understand the applicability of synthesized nanocomposite in the areas of supercapacitive energy storage & conversion, detailed electrochemical experiments were performed in a three-electrode probe

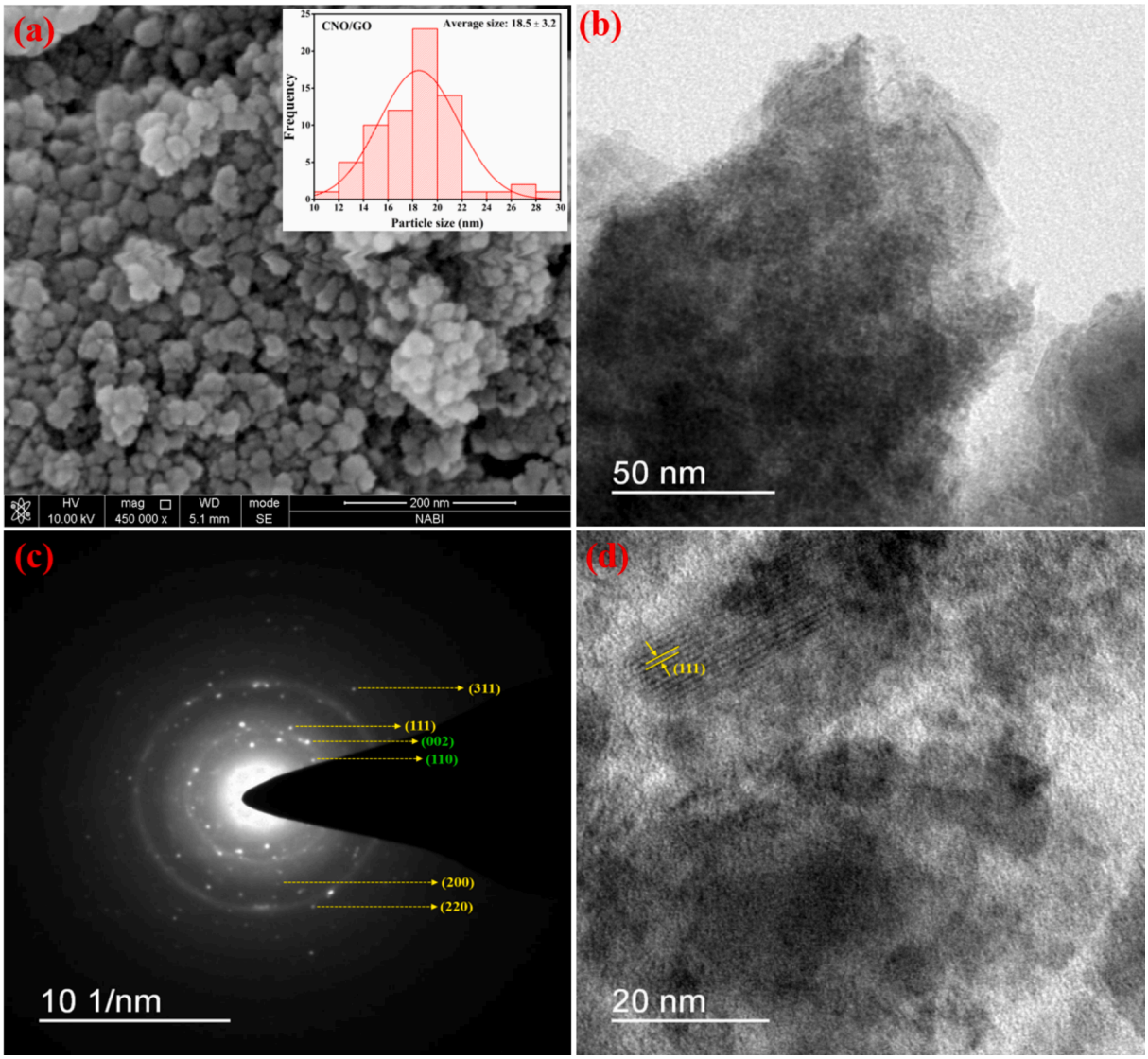

Fig. 3. Morphology investigation of CNO/GO nanocomposite via electron microscopy. (a) FE-SEM (inset showing particle size distribution), (b) TEM, (c) SAED, (d) HR-TEM analysis.

electrochemical workstation. The cyclic voltammetry (CV) analysis shown in Fig. 5a indicates the pseudocapacitive nature of the prepared CNO/GO nanocomposite. The redox peaks appeared within the 1-1.5 V potential window of CV, showing the quasi-reversible nature due to electrode polarization [13]. The gradual shift in anodic and cathodic peaks is due to the kinetic limitations of diffusing electrolytes through the electrode [5]. The associated faradic charge transfer via the redox mechanism is reversible since with an increase in voltage scan rate the current density gradually increased [67]. Increased current density values at high voltage scan rates indicate both the capacitive and faradic nature of voltammetry current [68].

The redox peaks appearing between 1-1.5 V RHE resulted from the influence of reversible intercalation and de-intercalation of OH^- ions into the CNO/GO nanocomposite present in 1M KOH electrolyte. Where the overall redox reaction can be represented accordingly [69,70].

$$NiO + OH^- \leftrightarrow NiOOH + e^- \quad (2)$$

The electrochemical activity of CNO/GO nanocomposite was further evaluated via measurement of the electrochemical active surface area (ESA). The measurement was based on the double layer capacitance (C_{dl}) in the nonfardic region of the CV plot while the voltage scan rate varied between 5 to 100 mV/s. The double-layer capacitance (C_{dl}) value was measured as 0.095 mF (Fig. S4a). By using Eq. (3), the ESA value accordingly calculated to be 2.37 cm^2 [71]. This shows the good intercalation support of the prepared nanocomposite for electrolyte ions under the faradic charge transfer mechanism. On the contrary, the electrochemical active surface area is estimated to be 0.95 cm^2 for as-synthesized GO.

$$ESA = C_{dl}/Cs \quad (3)$$

where $C_s = 40$ μF/cm^2 (specific capacitance of nickel foam used)

Further, the detailed charge storage mechanism involved in the CNO/GO nanocomposite as a supercapacitive electrode was investigated by a power law relation between cathodic peak current (Icp) Vs. voltage scan rate (ν) as suggested by Dunn. The resulting equation is mentioned in equations 4-5 [72]. Subsequent representation is shown in Fig. 5b.

$$I_{CP} = a\nu^b \quad (4)$$

$$\log_{10} I_{CP} = \log_{10} a + b\log_{10} \nu \quad (5)$$

The values of parameters (a, b) depicted in equation (3) are the result of a linear fitted equation (5). The two end limits of parameter 'b', such as 1 & 0, stand for capacitive & faradic (ion intercalation/de-intercalation) mechanisms, respectively, involved in the charge

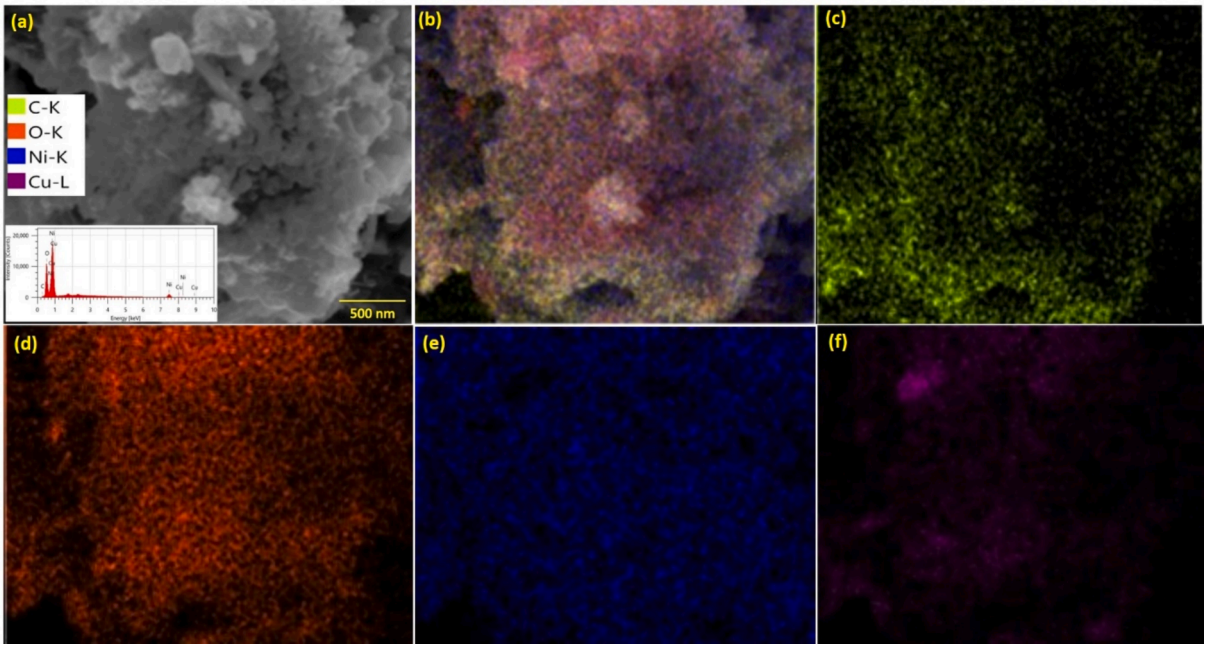

Fig. 4. EDX spectra & elemental mapping of CNO/GO nanocomposite indicate the purity of the prepared nanocomposite.

storage process as suggested by Cottrell's [73]. The linear fitting of equation (5), shown in the inset of Fig. 5b suggests that the value of b is obtained to be 0.52 in the current experiment. There is close agreement with the cathodic peak current densities calculated from equation (4) with modified a and b parameters and experimentally obtained values (Fig. 5b inset). Hence, the value of current density from the CV curve is pseudocapacitive in nature (linear combination of diffusion and surface redox reactions) [74]. However, in the current experiment diffusion of OH^- ions could have majorly contributed to the charge storage mechanism [73,75].

Further understanding of the charge storage contributions in the proposed pseudocapacitive CNO/GO nanocomposite was evaluated by the equation suggested by Dunn. As described by Dunn in equation (6), the capacitive contribution (K_1v) and diffusion contribution ($K_2v^{0.5}$) are two major mechanisms involved in pseudocapacitive charge storage. The values of K_1 and K_2 obtained from linear fitting of equation (7) (Fig. 5c). At a low scan rate (10 mV/s), the diffusion contribution towards charge storage is ~94 %, but this value decreases to ~80 % at high voltage sweeping (100 mV/s). This indicates capacitive mechanism also has observable contributions towards charge storage at a higher voltage sweeping rate (Fig. 5d & inset).

$$I(v) = K_1 v + K_2 v^{0.5} \tag{6}$$

$$I(v)/v^{0.5} = K_1 v^{0.5} + K_2 \tag{7}$$

The value of the specific capacitance resulting from the charge storage process in the CNO/GO nanocomposite electrode was obtained from the cyclic voltammetry curve by using equation (8).

$$C_s = \frac{A}{2mv\Delta V} \tag{8}$$

where C_s = Specific capacitance (F/g)

A = enclosed area within the CV curve

m = mass of active material used during electrode preparation

v= voltage scan rate (mV/s)

ΔV= potential window used for CV analysis

From the rate capacitance curve shown in Fig. 5a inset, it is observed that there is a decrease in specific capacitance value (363 F/g → 84 F/g) with an increase in voltage scan rate (5 mV/s → 100 mV/s). At a lower scan rate, there is a high residence time available for electrode-electrolyte interaction, thus high-capacity value is predicted, unlike the probability of limited diffusion of electrolyte ions at a high scan rate. The faradic charge transfer on the electrode surface could have played a pivotal role at a high scan rate. The trend observed in Fig. 5a is per the above-described phenomena, and an exponentially decreasing graph resulted [76,77].

For device applications, supercapacitive material in the electrode should have lower electronic resistance (or higher electrical conductivity)[78]. Electrochemical impedance spectroscopy (EIS) is an important characterization technique to investigate the conductivity of the prepared CNO/GO electrode, and the subsequent ion transfer kinetics influence the capacitance value at the electrode-electrolyte interface [76,79].

Fig. 6a shows the electrochemical impedance spectroscopy (EIS plot) of the synthesized CNO/GO nanocomposite under the influence of alternating current (AC). EIS of GO is also provided in the same figure for comparison purposes. The EIS plot mainly consists of the imaginary and real parts of the complex impedance data under varied AC frequencies [80]. The two incomplete semicircles at high to moderate frequency regions in the plot (Fig. 6a) can be credited to the varied faradic charge propagation phenomena occurring at the electrode-electrolyte interface. The expanded version of the semicircle at high-frequency region (inset Fig. 6a) shows the phenomena that occurred at the electrode-electrolyte interface, further modeled in terms of a circuit diagram (Fig. 6a inset) where resistance is in parallel with a constant phase element, Q (Zsimpwin circuit). As observed in the equivalent circuit, there exists a series resistance before the first semicircle that could be due to bulk electrolyte/electrode or contact resistance between electrode-current collector [81]. The ohmic resistance is lower in the case of CNO/GO (1.021 Ω) as compared to GO (1.651 Ω), indicating better contact of the nanocomposite-deposited electrode with the current collector. Besides, there is an observation of inductive resistance in the circuit that arises due to the collective contribution of the electronic components, such as electric connectors, cables, etc., used during measurement [82]. It is on a nanohenry scale and can be neglected. By the high electrochemical active surface area of the CNO/GO nanocomposite, supporting the faradic intercalation mechanism, the electrode resistance value associated with the first semicircle is very small (0.033 Ω), unlike the high

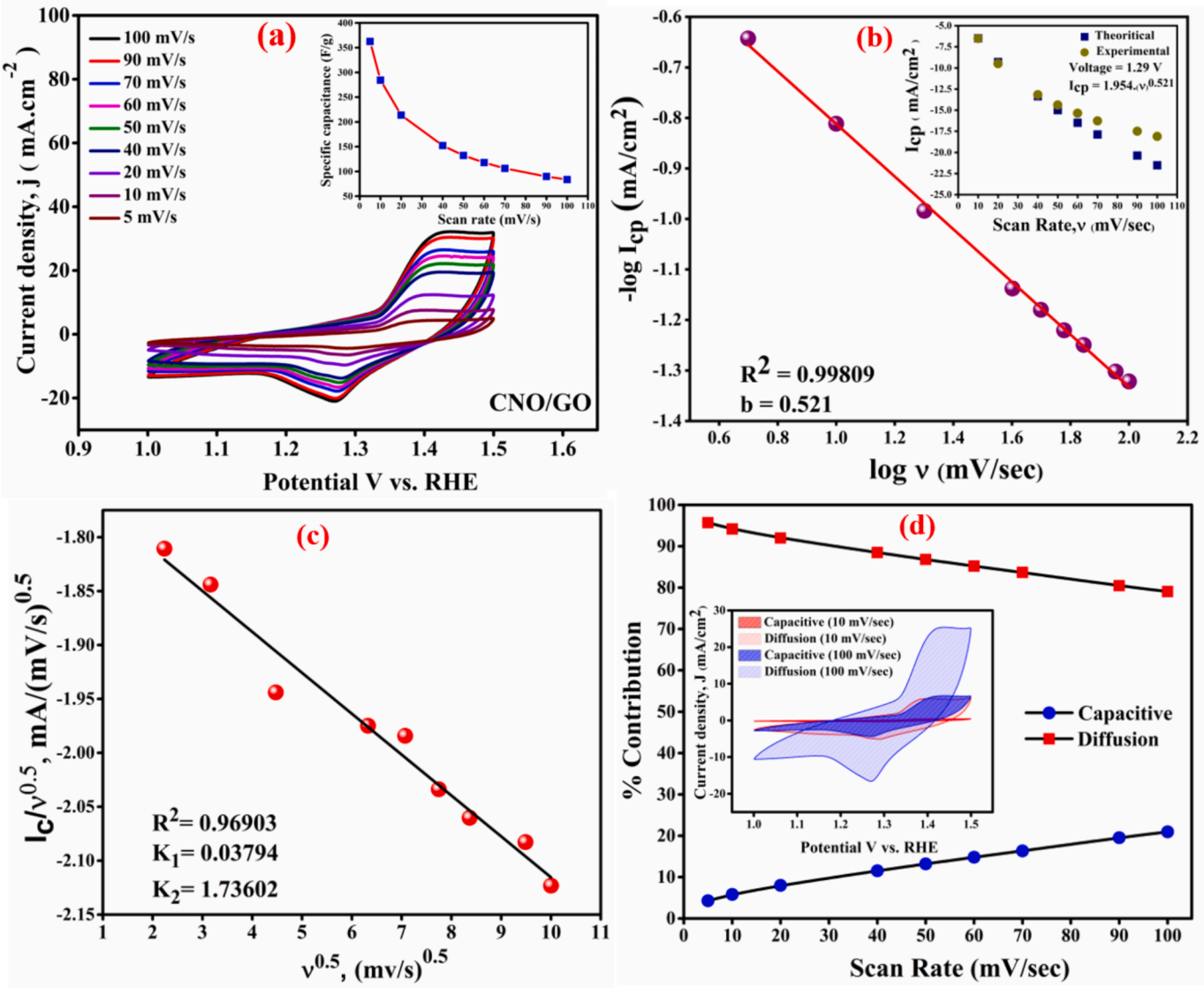

Fig. 5. Electrochemical characterizations and understanding of the charge storage mechanism of CNO/GO nanocomposite (a) cyclic Voltammetry analysis, (b) linear fitting of Dunn's equation, (c) & (d) understanding capacitive & diffusion effect in charge storage.

resistivity in the case of GO (2.287 Ω). Even the augmented value of the constant phase element in the case of GO indicates its EDLC-type behaviour with high capacitive impedance as compared to CNO/GO [83]. The second incomplete semicircle at a moderate frequency region could be due to the charge-transfer resistance (R_{CT}) experienced by the faradic redox process. This second semicircle can be modeled as "capacitance in parallel with resistance," mainly due to the faradic intercalation/de-intercalation of electrons and OH^- ions involved. The high resistance value obtained in the case of GO (336 Ω), unlike CNO/GO (~17.2 Ω), indicates that mainly surface phenomena contribute towards charge storage in the case of the former. Whereas the diffusion-controlled process is responsible in the case of the CNO/GO electrode.

The impedance (Z) and corresponding phase angle (Φ) of the CNO/GO electrode under AC applied frequency are simultaneously represented in a complex plane plot or Bode plot (Fig. 6b). From the bode plot, it can be observed that slope is < 1, which indicates pseudocapacitive nature of prepared nanocomposite [84]. Furthermore, the phase angle value ($\Phi = \sim 45^o$) deviating from the ideal capacitive behaviour ($\Phi = 90^o$) again supports the use of synthesized nanocomposite in the area of supercapacitors [85]. Comparatively, the Bode plot resulted in a high impedance slope and high phase angle ($\Phi = 55^o$) of 'GO' that led to its tendency towards a more capacitive mechanism in charge storage. (Fig. S4b)

A supercapacitor's performance index, e.g., energy density (E_S) and power density (P_S) can be assessed from the EIS data by showcasing the total capacitance value as a combination of both real (C') and imaginary (C'') components as mentioned in Eq. (9).

$$C(\omega) = C'(\omega) + C''(\omega) \tag{9}$$

where $C'(\omega) = -Z''(\omega)/\omega|Z(\omega)|^2$ and $C''(\omega) = Z'(\omega)/\omega|Z(\omega)|^2$

C' a describes the charge stored in the electrode as a function of frequency, which is nothing but E_S, and C'' stands for subsequent dissipation of stored charge. As shown in Fig. S4c, there is an asymptotic decrease in C' value with increased frequency. The variation in the C'' with frequency is slightly non-asymptotic with a point of inflection observed at frequency of 1.08 Hz (Fig. S4c inset). This peak frequency 'f_o' is termed as crossover frequency and beyond this supercapacitive material behaves as if to has a capacitive nature. On the contrary, in the case of GO, this value is 320 mHz (Fig. S4d). The charge relaxation time (τ), which is nothing but the reciprocal of the crossover frequency, quantitatively describes how fast a supercapacitor is discharged, or the power density [86]. In the current experiment, the value of 'τ' is

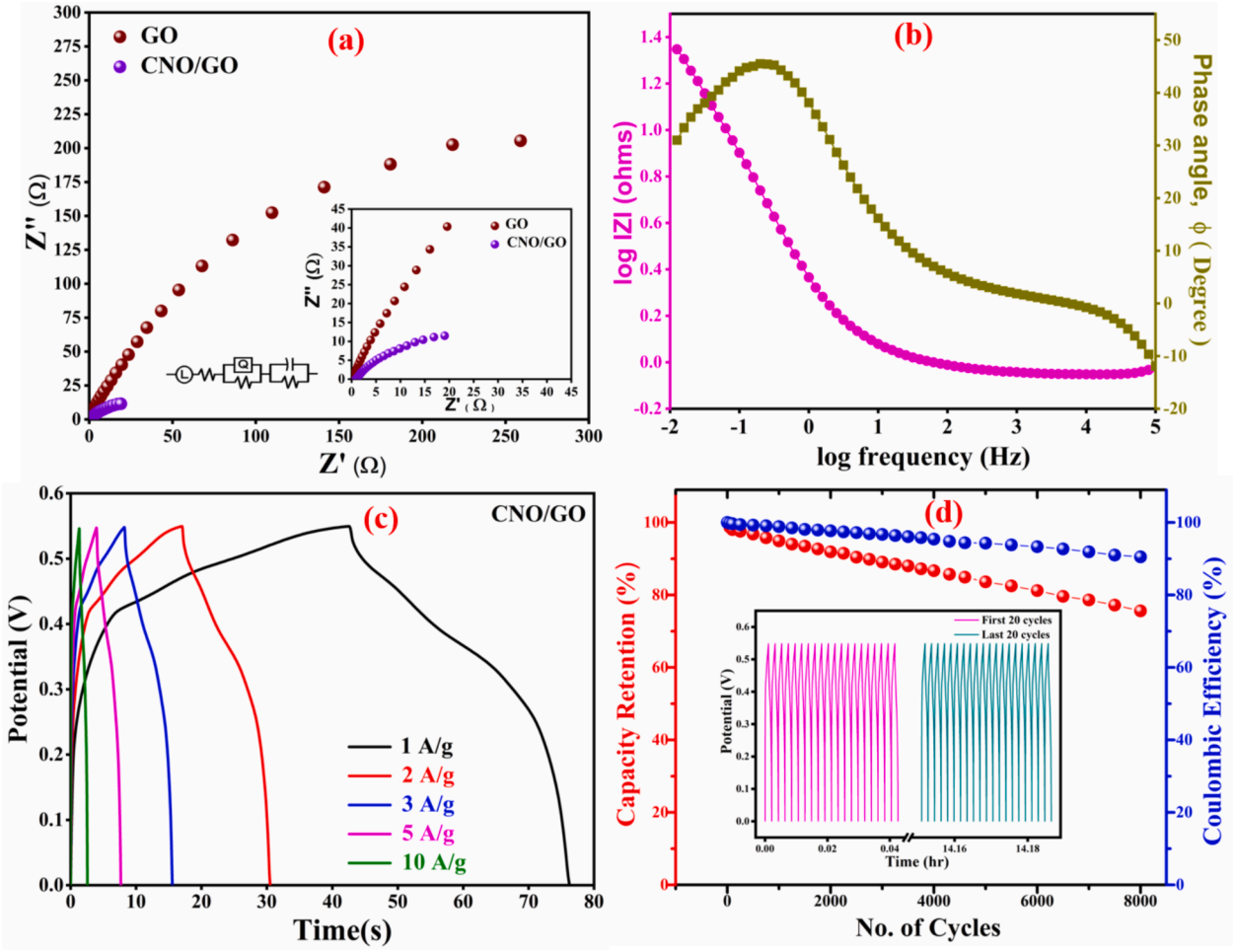

Fig. 6. (a) EIS, (b) Bode plot, (c) galvanostatic charge–discharge, (d) cyclic stability analysis of CNO/GO nanocomposite.

calculated as 0.92 s and 3.125 s for CNO/GO and GO electrodes, respectively. Hence synthesized CNO/GO nanocomposite as a super-capacitive electrode exhibits better power density as compared to GO alone.

The galvanostatic charge-discharge (GCD) characteristics of CNO/GO nanocomposite are shown in Fig. 6c. Due to the non-linearity that exists in the GCD curves drawn at different current densities, the pseudocapacitive behavior of the nanocomposite is again confirmed [87]. The slight initial voltage drop could have resulted as a consequence of multiple reasons, such as internal resistance of the electrode, resistance due to connectivity, ion diffusion resistance, bulk electrolyte resistance, etc. [86,88]. With variation in the current densities from 1 A/g → 10 A/g, the discharge time value decreases from 33.4 s to 1.2 s. Using the charge-discharge curve, the specific capacitance is evaluated using Eq. (10).

$$C_s = \frac{\mathbf{I} \times \mathbf{t_d}}{\mathbf{m} \times \Delta \mathbf{V}} \tag{10}$$

where C_s = specific capacitance (F/g)
t_d = discharging time
m = mass of active electrode material
ΔV = charge-discharge potential window

A high capacitance value (60.72 F/g) obtained at a low applied current density (1 A/g) is due to the concentration polarization effect. At small current density, low concentration polarization results in increased charging time. The abundance of ions in the vicinity of the electrode-electrolyte interface under the redox transition process is more probable, and hence, there is an augmented value of capacitance obtained. But at high current density (10 A/g), these effects are less probable, ultimately decreasing the specific capacitance value (21.8 F/g). All the values of specific capacitances obtained at different current densities are mentioned in Table 1. Even at a low current density of 1 A/g, the obtained specific capacity value is comparable with some of the earlier studies involving graphene-nickel oxide composites [89–91].

Equations (11) and (12) calculate the energy density (Es) and power density (Ps) characteristics of the synthesized nanocomposite.

$$E_s = \frac{1}{2} CV^2 (\mathrm{Wh/Kg}) \tag{11}$$

$$P_s = \frac{E_s}{t_d} (\mathrm{W/kg}) \tag{12}$$

Table 1
Specific capacitance, energy density, power density, and columbic efficiency of prepared nanocomposite from GCD curve both in 3-electrode (3Es) and 2-electrode (2Es) configurations.

Current Density (A/g)	C_S (F/g) 3Es	C_S (F/g) 2Es	~E_S (Wh/Kg) 3Es	E_S (Wh/Kg) 2Es	P_S (W/kg) 3Es	~P_S (W/kg) 2Es	η_c (%) 3Es
1	60.72	36.72	2.48	1.3	266.66	255	78.36
2	49.10	25.44	2.00	0.9	540.54	510	78.14
3	40.00	18	1.64	0.63	820.00	756	88.48
5	32.72	7.8	1.35	0.28	1350.00	1362	92.50
10	21.80	1.56	0.89	0.06	2966.66	1385	92.46

where C = specific capacitance (F/g), V = Voltage window (Volt), t_d = discharge time (s)

Though the energy density values observed in the synthesized nanocomposite are not so impressive, its pseudocapacitive nature has yielded higher power density values than earlier reported studies (Table 1). The current experiment resulted in a power density value of 266.66 W/Kg at a low current density of 1 A/g that can go up to 2966.6 W/Kg upon increasing the current density to 10 A/g. The power density of CNO/GO composite measured even at the low current density of 1 A/g is superior in comparison with earlier reported nanocomposites of carbonaceous material and nickel oxide [92–94]. Further, the coulombic efficiency (η) value of the supercapacitive electrode is estimated using Eq. (13) and represented in Table 1.

$$\eta\,(\%) = \frac{t_d}{t_c} \times 100 \tag{13}$$

where t_d and t_c are discharging and charging time respectively in sec

From Table 1, it is observed that the prepared CNO/GO composite exhibits a good coulombic efficiency of ~80 % and more. The variation or reduction in the Coulombic efficiency values might have been affected by one of several reasons, i.e., concentration polarization, irreversibility in the charging-discharging process, etc., and so on.

The three-electrode-based charge storage performance of different nanocomposite structures made up of multimetallic oxide and graphene is provided in Table 2. Under studied alkaline electrolytic conditions, the synthesized $Cu_{0.05}Ni_{0.95}O$/GO nanocomposite delivers good specific capacity and power density values. Moreover, the obtained specific capacity and power density are comparable to those of other reported work, even after using 1 M KOH as an electrolytic material and without incorporating additional conductive moieties for composite formation.

The stability of the CNO/GO pseudocapacitive electrode was ascertained by repeated cyclic measurements at a 50 mV/s scan rate. As shown in Fig. 6d, after 8000 cycles of repeated measurements, the capacitance retention is still maintained up to 75.6 %. Due to the involvement of the faradic redox process or chemical phenomena in the CNO/GO nanocomposite, upon repeated measurements, there could be wear & tear in the active electrode material, degradation of & volume change of the active material, electrolyte decomposition process, etc. [13]. Hence, there is a reduction in the specific capacitance retention value. On the other hand, in the case of GO alone, the EDLC-based electrostatic mechanism plays a crucial role in charge storage, where a high capacitance retention (~85 %) is achieved (Fig. S5). Moreover, the incorporation of GO into CNO/GO nanocomposite has led to the promotion of ion diffusion in the host CNO material and an increase in the specific surface area [97]. Thus, electrochemical stability could be established as a pseudocapacitive material. Further, the GCD time duration study in Fig. 6d inset shows the electrochemical stability of the prepared nanocomposite.

Table 2
Comparative 3-electrode-based electrochemical performances of different multimetal oxide and graphene composites under alkaline electrolytic conditions.

Material	Electrolyte	Cs (F/g) @ 1 A/g	E_S (Wh/Kg) @ 1 A/g	P_S (W/kg) @ 1 A/g	Ref.
rGO/Cu_2O	1 M KOH	33.3	–-	–-	[95]
Graphene/Co_3O_4	6 M KOH	163.5	–-	–-	[96]
rGO/Cu_2O/CuO	6 M KOH	173.4	–-	–-	[97]
GO/PANI/$CuCo_2O_4$	1 M KOH	308.15	62.54	300	[98]
NiO-rGO	6 M KOH	127.5	–-	–-	[91]
Vanadium nitride/GO	2 M KOH	109.7	–-	–-	[99]
$MnFe_2O_4$/GO	6 M KOH	298	–-	–-	[100]
$SmCoO_3$/rGO	2 M KOH	111	–-	–-	[101]
$Cu_{0.05}Ni_{0.95}O$/GO	1 M KOH	60.72	2.48	266.66	**Current Work**

3.3. Evaluation of charge storage performance via a coin cell device:

The active application of the electrochemical charge storage potential of the CNO/GO electrode was further ascertained via fabricating a coin cell device. The symmetric electrode configuration subjected to several electrochemical analyses (Fig. 7) revealed the potential of utilizing CNO/GO nanocomposite as a pseudocapacitive charge storage material. Cyclic voltammetry analysis (Fig. 7a) at a varied voltage scan rate between 5 to 90 mV/s suggests a pseudocapacitive nature. Further, a non-linear galvanostatic charge-discharge (GCD) plot (Fig. 7b) resulted due to the pseudocapacitive nature of the active material in the device, where the obtained specific capacity is as high as 36.75 F/g at an applied current density of 1 A/g (Table 1). This value is low in comparison to several other reported pieces of literature on graphene-metal oxide composites studied in a symmetric coin cell device mode [102–104].

However, the achieved value is promising without incorporating additional conducting moieties like polymer and reduced graphene oxide in the synthesized material, besides utilizing high electrolyte concentrations (> 1 M KOH) during electrochemical measurements. The practical applications of the fabricated device, evaluated in terms of energy and power density, revealed values of 1.3 Wh/kg and 255 W/Kg respectively (Table 1). Unlike energy density, the obtained power density value is comparable to the works of literature that tested coin cell efficacy under highly alkaline conditions (> 1 M KOH) and the incorporation of several conductive moieties as a third component in the synthesized composite [105]. Further, the cyclic stability of the device was tested for 8000 cycles at 50 mV/s voltage scan resulting in nearly 84 % capacity retention (Fig. 7C). Unlike a 3-electrode system, the closed environment achievable in coin cell device could be the main cause for high-capacity retention. The electrochemical impedance (EIS) study before and after entire cyclic operations (Fig. 7d) is an important criterion to comment on the application performances of fabricated devices in long-term use. The intercept of the EIS plot at the high-frequency region and semicircle combinedly stand for equivalent series resistance, ESR, which is the total of electrode resistance + electrolyte resistance + interfacial resistance + charge transfer resistance [106]. The ESR value before and after 8000 cycles of CV, as well as GCD operations, increased from its original value of 2.83 Ω to 9.19 Ω. All these factors interrelated with the material's stability and its bonding with the current collector are the main impediment towards decreased capacitance value. Moreover, the increase in ESR is not very high, which indicates the long-term electrochemical stability of prepared CNO/GO nanocomposite [107].

3.4. Electrocatalytic activity of CNO/GO nanocomposite:

Besides energy storage, electrochemical energy conversion for renewable fuel generation is another aspect of utilizing multimetallic oxide composites due to the greater achievable activity. This type of research is currently being explored largely to provide an efficient strategy for green hydrogen production via water splitting to reduce the dependency on fossil fuel usage. However, the water-splitting process to generate hydrogen is a hard task due to the involvement of a positive Gibbs free energy and a kinetic barrier. The use of suitable electrocatalysts downhill the process by overcoming these limitations. The performance of an electrocatalyst is evaluated in terms of its activity (overpotential, Tafel slope, exchange current density, etc.). Due to the significant kinetic barrier involved, the standard thermodynamic potential (1.23 V) in water splitting somehow rises to a higher value termed as overpotential (η). By using an electrocatalyst for this process, the overpotential value can be minimized. The overpotential is always calculated at a current density of 10 $mA.cm^{-2}$, exceeding 1.23 V. The Tafel slope weighs the activity of an electrocatalyst from the plot of

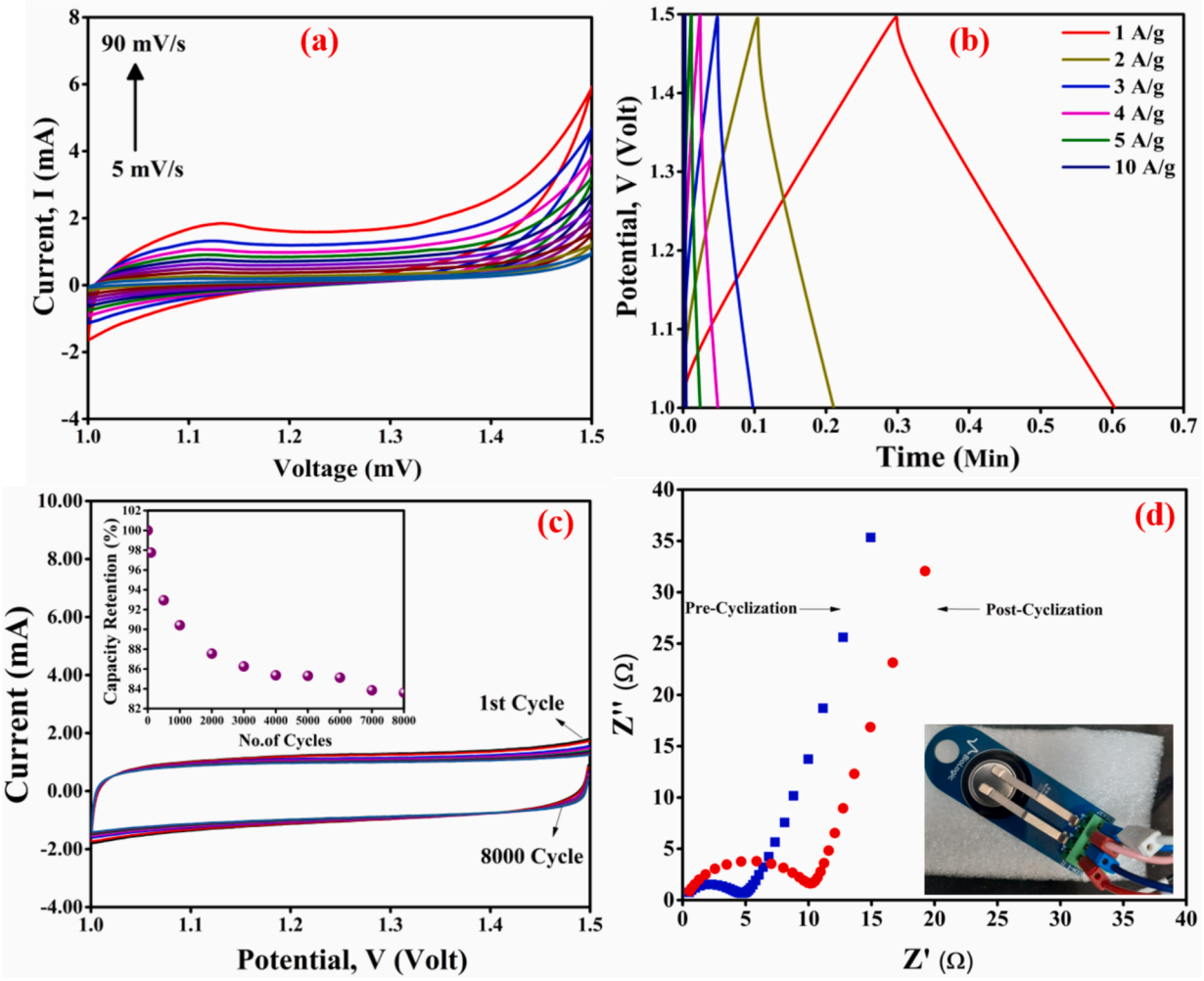

Fig. 7. Benchmarking of the electrochemical performance of CNO/GO nanocomposite via a symmetric coin cell fabrication. (a) CV data, (b) GCD at different current densities, (c) Cyclic stability of coin cell over 8000 cycles, (d) EIS data before and after the cyclic process.

overpotential vs. current density, in a kinetically controlled region. The overall relationship is expressed by equation (14).

$$\eta = a + b\log j \tag{14}$$

where η is the overpotential, and j is the current density

Tafel slope "b" is a function of electron-transfer kinetics. Smaller slope, faster electrocatalytic reaction kinetics. The value of exchange current density "j_o" can be decided by measuring the current at zero overpotential. "j_o" fundamentally describes intrinsic charge transfer under equilibrium. A high exchange current density means a high charge transfer rate and a low kinetic barrier for carrying out electrochemical water splitting.

There are two major mechanisms involved in water splitting: (i) Hydrogen evolution reaction (HER) and (ii) Oxygen evolution reaction (OER). HER half-reaction is accomplished at the cathode to generate hydrogen, unlike OER, which happens at the anode of the electrolytic cell and incurs high overpotential. It is inevitable for the OER reaction to occur at a lower overpotential value, which is directly related to the electrochemical activity of the chosen catalyst. The electrocatalytic OER-HER characteristics of the as-synthesized CNO/GO nanocomposite were examined via linear sweep voltammetry (LSV) at a voltage scan rate of 2 mV. s^{-1} in 1.0 M KOH electrolyte (Fig. 7a). For comparison, the activity of as-prepared GO is also provided in the same figure.

Fig. 8a shows the OER analysis of the CNO/GO nanocomposite. The as-synthesized composite exhibits a low onset potential (1.36 V Vs RHE) as compared to GO (V_{Onset}: 1.69 V) regarding a current density of 1 mA. cm^{-2}. Similarly, the overpotential value (η) to carry out OER using CNO/GO nanocomposite is lower (340 mV) as compared to the GO electrode (870 mV). This shows the exceptional activity of the prepared nanocomposite to carry out the OER reaction involved in the water splitting. The overpotential (η) value obtained in this current work is better as compared to other reported graphene-metallic oxide nanocomposites tested in 1 M KOH electrolyte, e.g., 430 mV [35], 379 mV [36], 430 mV [37], 313 mV [108], 450 mV [109].

Further, the low magnitude of the "Tafel" slope (49 mV/dec) in the case of CNO/GO nanocomposite obtained from the polarization graph (Fig. 8a inset) specifies faster electrocatalytic reaction kinetics, unlike GO, which has a "Tafel" slope of 165 mV/dec. Another confirmation of the improved electrocatalytic activity of the CNO/GO composite can be deduced from the exchange current density (I_{ex}) analysis of the OER Tafel slope. It is measured to be high, at 2.65E-5 in the case of CNO/GO nanocomposite, compared to GO, which has an "I_{ex}" value of 3.45E-6.

This was measured by linear extrapolation of the high current density region of the "Tafel" plot for V = 0. All such impressive OER results show better electrocatalytic efficiency of CNO/GO composite, which can be supported by earlier evaluated good electrochemical double layer capacitance of CNO/GO (0.095 mF). This double-layer capacitance can facilitate greater roughness in the prepared electrode, and thus, there is exposure of more active sites for better electrocatalytic performance [75]. The double-layer capacitance value is not so promising in the case of GO, having a value of 0.037 mF.

The HER study of CNO/GO nanocomposite (Fig. 8b) shows less

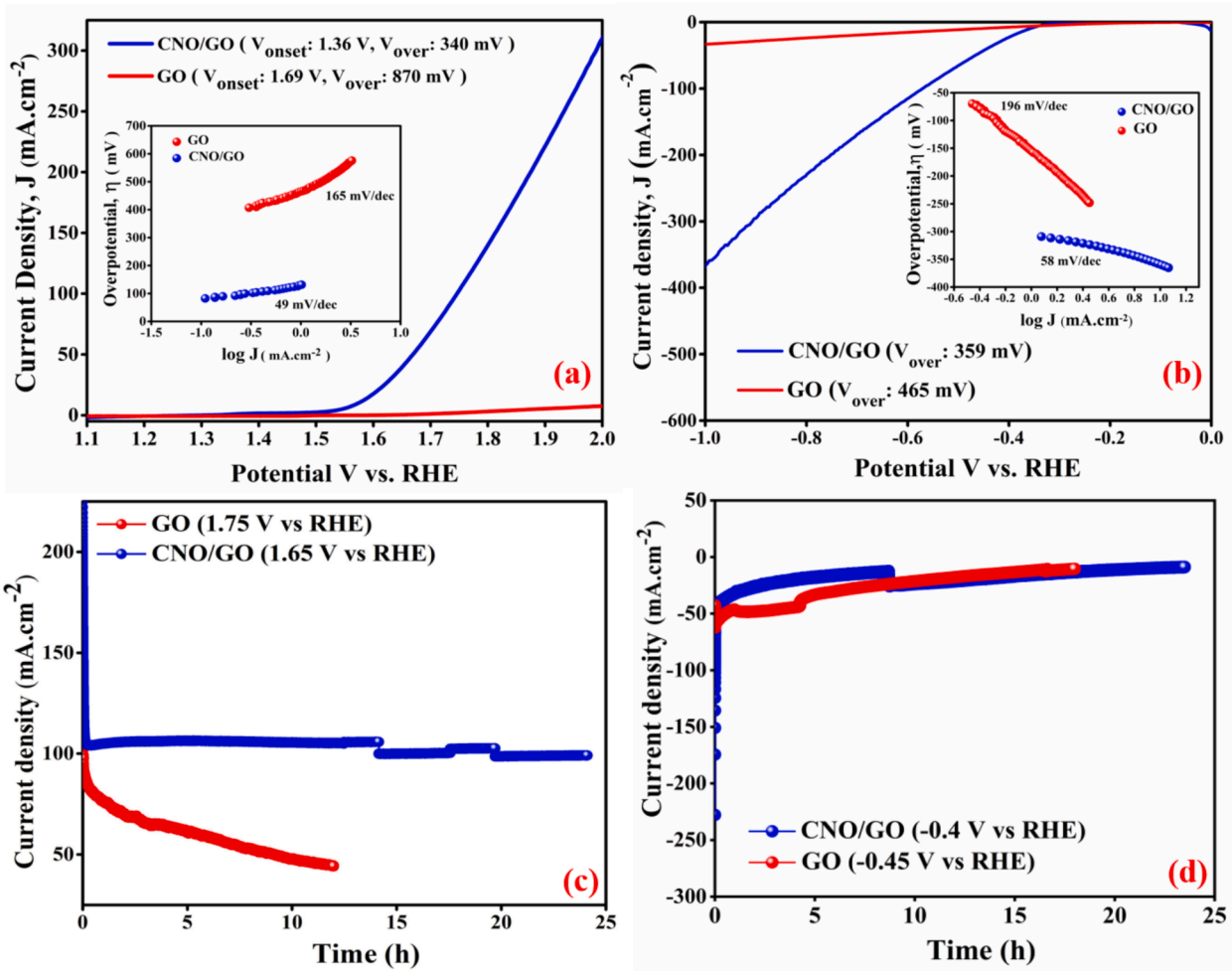

Fig. 8. Evaluating the electrocatalytic potential of CNO/GO nanocomposite. (a) LSV showing OER overpotential value. Inset showing corresponding Tafel slopes, (b) HER overpotential & corresponding Tafel slope (inset). Chronoamperometric stability test of the prepared CNO/GO nanocomposite (c) OER stability, (d) HER stability.

overpotential value: 359 mV, unlike GO, with an overpotential measured close to 465 mV. This indicates improved electrochemical activity achieved on composite formation towards hydrogen generation via water splitting. Further from the Fig. 8b inset, it can be corroborated that the prepared CNO/GO nanocomposite exhibits a faster electrocatalytic reaction rate as compared to GO, as the Tafel slope achieved is 58 mV/dec and 196 mV/dec in the case former and the latter, respectively. The comparative study between CNO/GO nanocomposite and some earlier reported pieces of literature on graphene-multimetallic oxide nanocomposites investigated as OER/HER electrocatalysts under 1M KOH electrolyte is provided in Table 3. From Table 3, it can be inferred that the currently explored material (CNO/GO) is an efficient electrocatalyst that can be simultaneously utilized as a dual OER-HER mode electrocatalyst based on its low overpotential and Tafel slope values.

Further, the electrocatalytic stability of the as-synthesized CNO/GO nanocomposite was investigated via chronoamperometric (CA) test against a bias voltage of 1.65 V and -0.40 V for OER and HER, respectively. Fig. 7c shows that at a current density of 100 mA cm^{-2}, the OER stability can be maintained up to 24 hours. Similarly, the HER stability of CNO/GO nanocomposite is observable in Fig. 7d without attenuation. On the contrary, graphene oxide alone cannot be stable under OER and HER catalytic operations under similar experimental conditions (Fig. 8c & d). All these results indicate the stability & robustness of the prepared nanocomposite towards the electrocatalysis process via a synergistic combination between multimetallic oxides and graphene oxide

Table 3
OER/HER electrocatalytic potential of earlier reported multimetallic oxide-graphene nanocomposites studied under 1 M KOH conditions.

Electrocatalyst	OER, η (mV)	~Tafel Slope (mV/dec)	HER, η (mV)	~Tafel Slope (mV/dec)	Ref.
Cobalt-Manganese Oxide/Graphene	430	55	–-	–-	[35]
GO/MnO_2–NiO	379	48	–-	–-	[36]
NrGO/$Cu_xCo_{3-x}O_4$	270	63	170	85	[43]
CuO/NiO/rGO	200	165	–-	–-	[45]
rGO/CO_3O_4	410	85	–-	–-	[109]
Co_3O_4/rGO	346	47	–-	–-	[110]
α-$Co(OH)_2$/PPy/GO	350	75	–-	–-	[111]
$Co_{1-x}Ni_xFe_2O_4$/rGO	440	85	–-	–-	[112]
RGO-NiO/Ni	530	81	–-	–-	[113]
NrGO/$CuCo_2O_4$	360	64	–-	–-	[114]
NrGO/Co_3O_4	400	57	–-	–-	[114]
rGO/CuO/ZnO	1678	42	358	270	[115]
$Cu_{0.05}Ni_{0.95}O$/GO	340	49	359	58	**Current Work**

[108,109,116]. These results are consistent with the electrochemical active surface area (ESA) measurement stated earlier, both for GO and CNO/GO. Henceforth, the prepared CNO/GO nanocomposite seems to be a promising material for carrying out electrocatalytic reactions.

4. Conclusion

Current work demonstrates a facile way of synthesizing copper-nickel bimetallic oxide nanocomposite coexisting with GO ($Cu_{0.05}Ni_{0.95}O$/GO) by simple thermal reduction for establishing the electrochemical potentials. The electrochemical charge storage ability was evaluated via CV and the EIS techniques. This study suggests the pseudocapacitive charge storage nature of the prepared nanocomposite, where the faradic redox/ion intercalation mechanism majorly (~94 %) contributes. The galvanostatic charge–discharge further resulted in a power density of 267 W/Kg with 1 A/g applied current density, which is comparable or higher to earlier reported works on composite structures. Besides, the symmetric coin cell configuration resulted in specific capacity and power density of 37F/g and 255 W/Kg respectively. The concurrent electrocatalytic potential of the prepared nanocomposite was evaluated through overpotential measurements from LSV, exhibiting lower values of 340 mV and 359 mV for OER and HER, respectively. All such characteristics establish the multiple applicability of the CNO/GO nanocomposite in electrochemical energy storage and energy generation prospects cited under the current era of renewable energy research.

Data availability: All data used in this study are represented in this manuscript and provided in the electronic supplementary information.

CRediT authorship contribution statement

Kedar Sahoo: Writing – review & editing, Writing – original draft, Visualization, Validation, Software, Methodology, Investigation, Formal analysis, Data curation, Conceptualization. **Deepak Kumar:** Validation, Software, Formal analysis. **Vishal K. Kushwaha:** Software, Resources, Investigation. **Ajinkya Kotkar:** Methodology, Formal analysis, Data curation. **Arindam Indra:** Writing – review & editing, Supervision, Software, Resources. **Shirish H. Sonawane:** Writing – review & editing, Supervision, Resources, Funding acquisition. **Suddhasatwa Basu:** Writing – review & editing, Supervision, Resources, Project administration.

Declaration of competing interest

The authors declare that they have no known competing financial interests or personal relationships that could have appeared to influence the work reported in this paper.

We would like to thank NRF IITD, Fuel Cell Lab IITD, and CRIF NITW for providing materials characterization facilities.

Appendix A. Supplementary data

Supplementary data to this article can be found online at https://doi.org/10.1016/j.mseb.2025.118425.

Data availability

Data will be made available on request.

References

[1] T. Ahmad, D. Zhang, Energy Rep. 6 (2020) 1973–1991.
[2] G. Oroumi, R. Monsef, E.A. Dawi, A.M. Aljeboree, M.H.S. Alubiady, A.M. Al-Ani, M. Salavati-Niasari, J. Storage Mater. 85 (2024) 111161.
[3] P.-P. Liu, Y.-Q. Zheng, H.-L. Zhu, T.-T. Li, ACS Appl. Nano Mater. 2 (2019) 744–749.
[4] Z. Heydariyan, M. Salavati-Niasari, R. Monsef, Fuel 372 (2024) 132177.
[5] K. Sahoo, N. Varshney, T. Das, S.K. Mahto, M. Kumar, Appl. Nanosci. (2023) 1–22.
[6] J.K. Das, A.K. Samantara, S. Satyarthy, C.S. Rout, J. Behera, RSC Adv. 10 (2020) 4650–4656.
[7] K. Chaudhary, S. Zulfiqar, H. Somaily, M. Aadil, M.F. Warsi, M. Shahid, Electrochim. Acta 431 (2022) 141103.
[8] M. Aadil, A.G. Taki, S. Zulfiqar, A. Rahman, M. Shahid, M.F. Warsi, Z. Ahmad, A. A. Alothman, S. Mohammad, RSC Adv. 13 (2023) 28063–28075.
[9] S. Ramesh, K. Karuppasamy, D. Vikraman, P. Santhoshkumar, C. Bathula, R. R. Palem, A. Kathalingam, H.-S. Kim, J.-H. Kim, H.S. Kim, J. Alloy. Compd. 892 (2022) 162182.
[10] M. Kigozi, R.K. Koech, O. Kingsley, I. Ojeaga, E. Tebandeke, G.N. Kasozi, A. P. Onwualu, Results in Materials 7 (2020) 100113.
[11] L.L. Zhang, X. Zhao, Chem. Soc. Rev. 38 (2009) 2520–2531.
[12] N. Arshad, M. Usman, M. Adnan, M.T. Ahsan, M.R. Rehman, S. Javed, Z. Ali, M. A. Akram, G.P. Demopoulos, A. Mahmood, Nanomaterials 13 (2022) 99.
[13] V. Senthilkumar, Y.S. Kim, S. Chandrasekaran, B. Rajagopalan, E.J. Kim, J. S. Chung, RSC Adv. 5 (2015) 20545–20553.
[14] C. An, Y. Zhang, H. Guo, Y. Wang, Nanoscale Adv. 1 (2019) 4644–4658.
[15] T.E. Balaji, H. Tanaya Das, T. Maiyalagan, ChemElectroChem 8 (2021) 1723–1746.
[16] J.W. Crawley, I.E. Gow, N. Lawes, I. Kowalec, L. Kabalan, C.R.A. Catlow, A. J. Logsdail, S.H. Taylor, N.F. Dummer, G.J. Hutchings, Chem. Rev. 122 (2022) 6795–6849.
[17] K. Zhang, W. Zeng, G. Zhang, S. Hou, F. Wang, T. Wang, H. Duan, RSC Adv. 5 (2015) 69636–69641.
[18] S.C. Sekhar, G. Nagaraju, J.S. Yu, Nano Energy 48 (2018) 81–92.
[19] A. Pendashteh, S.E. Moosavifard, M.S. Rahmanifar, Y. Wang, M.F. El-Kady, R. B. Kaner, M.F. Mousavi, Chem. Mater. 27 (2015) 3919–3926.
[20] A. Irshad, S. Zulfiqar, Z.A. Alothman, I. Shakir, M.F. Warsi, E.W. Cochran, Fuel 362 (2024) 130705.
[21] S. Thekkoot, R. Islam, O. Gray, S. Morin, Electrochim. Acta 471 (2023) 143339.
[22] B. Chi, H. Lin, J., Li, International Journal of Hydrogen Energy 33 (2008) 4763–4768.
[23] A. Rebekah, E.A. Kumar, C. Viswanathan, N. Ponpandian, Int. J. Hydrogen Energy 45 (2020) 6391–6403.
[24] J. Qiao, F. Song, J. Hu, D. Huo, J. Yuan, J. Shen, L. Niu, A.-J. Wang, Int. J. Hydrogen Energy 44 (2019) 16368–16377.
[25] G.A. Gebreslase, M.V. Martínez-Huerta, M.J. Lázaro, Journal of Energy Chemistry 67 (2022) 101–137.
[26] B.J. Rani, S. Pradeepa, Z.M. Hasan, G. Ravi, R. Yuvakkumar, S. Hong, J. Phys. Chem. Solid 138 (2020) 109240.
[27] S. Anantharaj, S. Kundu, S. Noda, Nano Energy 80 (2021) 105514.
[28] J. Kundu, S. Khilari, K. Bhunia, D. Pradhan, Cat. Sci. Technol. 9 (2019) 406–417.
[29] Z. Liu, G. Wang, X. Zhu, Y. Wang, Y. Zou, S. Zang, S. Wang, Angew. Chem. 132 (2020) 4766–4772.
[30] A. La Rosa-Toro, R. Berenguer, C. Quijada, F. Montilla, E. Morallón, J. Vázquez, J. Phys. Chem. B 110 (2006) 24021–24029.
[31] M.A.A.M. Abdah, N.H.N. Azman, S. Kulandaivalu, Y. Sulaiman, Mater. Des. 186 (2020) 108199.
[32] S. Ramesh, K. Karuppasamy, A. Sivasamy, H.-S. Kim, H. Yadav, H.S. Kim, J. Alloy. Compd. 877 (2021) 160297.
[33] V. Kakani, S. Ramesh, H.M. Yadav, A. Kumar, S. Shinde, S. Sandhu, L.N.D. Quang, H.S. Kim, H.-S. Kim, H. Kim, J. Alloy. Compd. 847 (2020) 156411.
[34] Q. Pang, Y. Zhao, X. Bian, Y. Ju, X. Wang, Y. Wei, B. Liu, F. Du, C. Wang, G. Chen, J. Mater. Chem. A 5 (2017) 3667–3674.
[35] H. Kobayashi, Y. Sugawara, T. Yamaguchi, I. Honma, Chem. Commun. 57 (2021) 9052–9055.
[36] S.P. Mooni, K.K. Kondamareddy, S. Li, X. Zhou, L. Chang, X. Ke, X. Yang, D. Li, Q. Qu, Arab. J. Chem. 13 (2020) 4553–4563.
[37] Y. Xiao, B. Guo, J. Zhang, C. Hu, R. Ma, D. Wang, J. Wang, Dalton Trans. 49 (2020) 5730–5735.
[38] M. Lu, Y. Cao, Y. Xue, W. Qiu, ACS Omega 6 (2021) 27994–28003.
[39] T. Kavinkumar, K. Vinodgopal, B. Neppolian, Appl. Surf. Sci. 513 (2020) 145781.
[40] B. Bashir, A. Rahman, H. Sabeeh, M.A. Khan, M.F.A. Aboud, M.F. Warsi, I. Shakir, P.O. Agboola, M. Shahid, Ceram. Int. 45 (2019) 6759–6766.
[41] A. Umar, M.S. Akhtar, S. Ameen, M. Imran, R. Kumar, Y. Wang, A.A. Ibrahim, H. Albargi, M. Jalalah, M.A. Alsaiari, Microchem. J. 160 (2021) 105630.
[42] D.S. Nair, A. Anil, L. Elias, N. Satyanarayana, H.K. Holla, S. Shibli, Int. J. Hydrogen Energy 62 (2024) 162–171.
[43] T. Niyitanga, H. Kim, J. Power Sources 580 (2023) 233383.
[44] J. Balamurugan, T.D. Thanh, S.-B. Heo, N.H. Kim, J.H. Lee, Carbon 94 (2015) 962–970.
[45] P. Mohana, R. Yuvakkumar, G. Ravi, S. Arunmetha, Electrochim. Acta 473 (2024) 143464.
[46] N.X.A. Nguyen, T.K.N. Nguyen, T.N. Pham, T.T. Nguyen, T.T.T. Nguyen, N. T. Hoang, T. Dai Lam, RSC Adv. 11 (2021) 28573–28580.
[47] B. Liu, X. Ouyang, Y. Ding, L. Luo, D. Xu, Y. Ning, Talanta 146 (2016) 114–121.
[48] C.R. Dhas, S.E.S. Monica, K. Jothivenkatachalam, A.J. Nathanael, V. Kavinkumar, R. Venkatesh, D. Arivukarasan, Ionics (2021) 1–14.
[49] B. Demirkan, S. Bozkurt, A. Şavk, K. Cellat, F. Gülbağca, M.S. Nas, M.H. Alma, F. Sen, Sci. Rep. 9 (2019) 12258.
[50] M.J. Uddin, M.S. Yeasmin, A.A. Muzahid, M.M. Rahman, G.M. Rana, T. A. Chowdhury, M. Al-Amin, M.K. Wakib, S.H. Begum, Heliyon 10 (2024).
[51] J. Wu, X. Shen, L. Jiang, K. Wang, K. Chen, Appl. Surf. Sci. 256 (2010) 2826–2830.
[52] R. Tariq, S. Zulfiqar, H. Somaily, M.F. Warsi, I. Ayman, F. Hanif, M. Akhtar, M. Aadil, Surf. Interfaces 34 (2022) 102350.
[53] S. Jharwal, P.K. Singh, D.K. Rana, M.K. Srivastava, A. Kumar, Mater. Today Proc. 67 (2022) 648–651.
[54] N. Hidayah, W.-W. Liu, C.-W. Lai, N. Noriman, C.-S. Khe, U. Hashim, H.C. Lee, AIP Conference Proceedings, AIP Publishing (2017).

[55] Y. Wan, L. Chen, W. Tang, J. Li, J. Mater. Res. Technol. 9 (2020) 3796–3804.
[56] V. Modafferi, S. Santangelo, M. Fiore, E. Fazio, C. Triolo, S. Patanè, R. Ruffo, M. G. Musolino, J. Nanomater. 2019 (2019) 1703218.
[57] A. Valipour, N. Hamnabard, Y.-H. Ahn, RSC Adv. 5 (2015) 92970–92979.
[58] S. Chandra, D. Bano, K. Sahoo, D. Kumar, V. Kumar, P.K. Yadav, S.H. Hasan, Microchem. J. 172 (2022) 106953.
[59] M. Cheng, H. Fan, Y. Song, Y. Cui, R. Wang, Dalton Trans. 46 (2017) 9201–9209.
[60] W. Liu, C. Lu, X. Wang, K. Liang, B.K. Tay, J. Mater. Chem. A 3 (2015) 624–633.
[61] M. Yin, C.-K. Wu, Y. Lou, C. Burda, J.T. Koberstein, Y. Zhu, S. O'Brien, J. Am. Chem. Soc. 127 (2005) 9506–9511.
[62] C.-K. Wu, M. Yin, S. O'Brien, J.T. Koberstein, Chem. Mater. 18 (2006) 6054–6058.
[63] M.C. Biesinger, L.W. Lau, A.R. Gerson, R.S.C. Smart, Appl. Surf. Sci. 257 (2010) 887–898.
[64] B. Paulchamy, G. Arthi, B. Lignesh, J Nanomed Nanotechnol 6 (2015) 1.
[65] V. Loryuenyong, K. Totepvimarn, P. Eimburanapravat, W. Boonchompoo, A. Buasri, Adv. Mater. Sci. Eng. 2013 (2013).
[66] S. Eigler, C. Dotzer, A. Hirsch, M. Enzelberger, P. Müller, Chem. Mater. 24 (2012) 1276–1282.
[67] S.K. Hussain, G. Nagaraju, S.C. Sekhar, J.S. Yu, J. Power Sources 439 (2019) 227088.
[68] T. Das, B. Verma, J. Storage Mater. 26 (2019) 100975.
[69] Q. Li, C.-L. Li, Y.-L. Li, J.-J. Zhou, C. Chen, R. Liu, L. Han, Inorg. Chem. Commun. 86 (2017) 140–144.
[70] J. Yin, J.Y. Park, Int. J. Hydrogen Energy 39 (2014) 16562–16568.
[71] Y.K. Li, G. Zhang, W.T. Lu, F.F. Cao, Adv. Sci. 7 (2020) 1902034.
[72] M. Aadil, S. Zulfiqar, M. Shahid, P.O. Agboola, S. Haider, M.F. Warsi, I. Shakir, J. Electroanal. Chem. 884 (2021) 115070.
[73] A. Gupta, V. Kushwaha, R. Mondal, A.N. Singh, R. Prakash, K. Mandal, P. Singh, PCCP 24 (2022) 11066–11078.
[74] X. Zhu, J. Storage Mater. 49 (2022) 104148.
[75] Z. Wang, J. Chen, R. Bi, W. Dou, K. Wang, F. Mao, H. Wu, S. Wang, J. Solid State Chem. 283 (2020) 121128.
[76] B. Vidhyadharan, I.I. Misnon, R. Abd Aziz, K. Padmasree, M.M. Yusoff, R. Jose, J. Mater. Chem. A 2 (2014) 6578–6588.
[77] S.K. Shinde, D.P. Dubal, G.S. Ghodake, V.J. Fulari, RSC Adv. 5 (2015) 4443–4447.
[78] S.K. Meher, P. Justin, G.R. Rao, Nanoscale 3 (2011) 683–692.
[79] Y.X. Zhang, M. Huang, F. Li, Z.Q. Wen, Int. J. Electrochem. Sci 8 (2013) 8645–8661.
[80] M. Aadil, S. Zulfiqar, P.O. Agboola, M.F.A. Aboud, I. Shakir, M.F. Warsi, Synth. Met. 272 (2021) 116645.
[81] B.-A. Mei, O. Munteshari, J. Lau, B. Dunn, L. Pilon, J. Phys. Chem. C 122 (2018) 194–206.
[82] I.M. Badawy, A.M. Elbanna, M. Ramadan, N.K. Allam, Electrochim. Acta 408 (2022) 139932.
[83] M. Schalenbach, Y.E. Durmus, H. Tempel, H. Kungl, R.-A. Eichel, PCCP 23 (2021) 21097–21105.
[84] A.S. ELmezayyen, S. Guan, F.M. Reicha, I.M. El-Sherbiny, C. Xu, Journal of Physics D: Applied Physics, 48 (2015) 175502.
[85] X. Fuku, M. Modibedi, M. Mathe, SN Appl. Sci. 2 (2020) 1–15.
[86] Y. Lu, H. Yan, K. Qiu, J. Cheng, W. Wang, X. Liu, C. Tang, J.-K. Kim, Y. Luo, RSC Adv. 5 (2015) 10773–10781.
[87] T. Das, B. Verma, J. Mater. Sci. Mater. Electron. 33 (2022) 12734–12749.
[88] A. Pendashteh, M.F. Mousavi, M.S. Rahmanifar, Electrochim. Acta 88 (2013) 347–357.
[89] S. Haider, R. Abid, I. Murtaza, A. Shuja, ACS Omega 8 (2023) 46002–46012.
[90] E.S. Agudosi, E.C. Abdullah, A. Numan, N.M. Mubarak, S.R. Aid, R. Benages-Vilau, P. Gómez-Romero, M. Khalid, N. Omar, Sci. Rep. 10 (2020) 11214.
[91] J. Xu, L. Wu, Y. Liu, J. Zhang, J. Liu, S. Shu, X. Kang, Q. Song, D. Liu, F. Huang, Surf. Interfaces 18 (2020) 100420.
[92] N. Parveen, G.M. Alsulaim, S.A. Alsharif, H.H. Almutairi, H.A. Alali, S.A. Ansari, M.M. Ahmad, J. Sci.: Adv. Mater. Devices 8 (2023) 100591.
[93] A. Shah, S. Senapati, H.A. Murthy, L.R. Singh, M. Mahato, ACS Omega 8 (2023) 33380–33391.
[94] R.M. Obodo, S.M. Mbam, H.E. Nsude, M. Ramzan, S.C. Ezike, I. Ahmad, M. Maaza, F.I. Ezema, Appl. Surf. Sci. Adv. 9 (2022) 100254.
[95] X. Dong, K. Wang, C. Zhao, X. Qian, S. Chen, Z. Li, H. Liu, S. Dou, J. Alloy. Compd. 586 (2014) 745–753.
[96] W. Zhou, J. Liu, T. Chen, K.S. Tan, X. Jia, Z. Luo, C. Cong, H. Yang, C.M. Li, T. Yu, PCCP 13 (2011) 14462–14465.
[97] K. Wang, X. Dong, C. Zhao, X. Qian, Y. Xu, Electrochim. Acta 152 (2015) 433–442.
[98] S. Verma, V.K. Pandey, B. Verma, Synth. Met. 286 (2022) 117036.
[99] T. He, Z. Wang, X. Li, Y. Tan, Y. Liu, L. Kong, L. Kang, C. Chen, F. Ran, J. Alloy. Compd. 781 (2019) 1054–1058.
[100] N. Foroutan, M.S. Lashkenari, E. Alizadeh, M. Sedighi, Int. J. Hydrogen Energy 48 (2023) 25859–25868.
[101] M. Isacfranklin, R. Yuvakkumar, G. Ravi, S. Hong, D. Velauthapillai, M. Thambidurai, C. Dang, T.S. Algarni, A.M. Al-Mohaimeed, Carbon 172 (2021) 613–623.
[102] G. Sriram, M. Arunpandian, K. Dhanabalan, V.R. Sarojamma, S. David, M. D. Kurkuri, T.H. Oh, Inorganics 12 (2024) 145.
[103] A. Kumar, H.K. Rathore, D. Sarkar, A. Shukla, Electrochem. Sci. Adv. 2 (2022) e2100187.
[104] P. Pazhamalai, V. Krishnan, M.S. Mohamed Saleem, S.-J. Kim, H.-W. Seo, Nano Convergence 11 (2024) 30.
[105] R. Lakra, R. Kumar, P.K. Sahoo, D. Thatoi, A. Soam, Inorg. Chem. Commun. 133 (2021) 108929.
[106] Q. Abbas, L. Wen, M.S. Javed, A. Ahmad, M.S. Nazir, M.A. Assiri, M. Imran, P. Bocchetta, Materials 15 (2022) 2250.
[107] A.E. Elkholy, A.S. Dhmees, F.-E.-T. Heakal, M. Deyab, New J. Chem. 43 (2019) 1987–1992.
[108] Y. Zhao, S. Chen, B. Sun, D. Su, X. Huang, H. Liu, Y. Yan, K. Sun, G. Wang, Sci. Rep. 5 (2015) 7629.
[109] Z. Wu, L.-P. Sun, M. Yang, L.-H. Huo, H. Zhao, J.-C. Grenier, J. Mater. Chem. A 4 (2016) 13534–13542.
[110] M. Leng, X. Huang, W. Xiao, J. Ding, B. Liu, Y. Du, J. Xue, Nano Energy 33 (2017) 445–452.
[111] H. Mao, X. Guo, Y. Fu, Z. Cao, D. Sun, B. Wang, Y. Zhang, Q. Fan, X.-M. Song, Appl. Surf. Sci. 485 (2019) 554–563.
[112] I. Madakannu, I. Patil, B.A. Kakade, K.R.D. Kasibhatta, Mater. Chem. Phys. 252 (2020) 123238.
[113] D. Wang, F. Watanabe, W. Zhao, ECS J. Solid State Sci. Technol. 6 (2017) M3049.
[114] S.K. Bikkarolla, P. Papakonstantinou, J. Power Sources 281 (2015) 243–251.
[115] U. Younas, F. Mobeen, A. Saleem, F. Ali, M. Al Huwayz, A. Ashraf, A. Ahmad, N. Alwadai, M. Pervaiz, M. Iqbal, Ceram. Int. (2024).
[116] X. Xu, Q. An, H. Sun, Y. Wang, W. Shang, L. Bao, Z. Jia, Q. Zhang, New J. Chem. 45 (2021) 19852–19857.